*Korean J. Chem. Eng.*, 37(8), 1317-1330 (2020)
DOI: 10.1007/s11814-020-0612-4

pISSN: 0256-1115
eISSN: 1975-7220

**INVITED REVIEW PAPER**

# Development strategies in transition metal carbide for hydrogen evolution reaction: A review

**Hyunwoo Jun*,‡, Seongbeen Kim*,**,‡, and Jinwoo Lee*,†**

*Department of Chemical and Biomolecular Engineering, Korea Advanced Institute of Science and Technology (KAIST), 291 Daehak-ro, Daejeon 34141, Korea
**Department of Chemical Engineering, Pohang University of Science and Technology (POSTECH), 77 Cheongam-ro, Nam-gu, Pohang, Gyeongbuk 37673, Korea
(*Received 27 April 2020 • Revised 28 May 2020 • Accepted 8 June 2020*)

**Abstract**−Economically viable hydrogen production by water electrolysis requires an inexpensive and efficient electrocatalyst. Transition metal carbides (TMCs) have many merits such as low price, platinum-like catalytic activity, high physical stability, and electrical conductivity. This review presents strategies for improving the catalytic activity of TMCs. It highlights synthesis using nanostructuring by inorganic-organic complexes and carbon supports to increase the number of active sites and to facilitate mass transport, and modification of electronic configuration by heteroatom doping, heterostructure, and phase control to increase intrinsic activity. The review concludes with an outlook on challenges to achieving practical TMC catalysts for the hydrogen evolution reaction.

Keywords: Inorganic-organic Complex, Carbon Support, Heteroatom Doping, Heterostructure, Phase Control

## INTRODUCTION

Exponentially increasing consumption of fossil fuels has caused serious environmental deterioration for the past century. Along with the limited reserves problem, the development of sustainable alternative energy source is inevitable. Renewable energies (e.g., solar, wind, tidal, hydroelectric power) are options but they are restricted to spatial and intermittency problems. Hydrogen is an ideal energy carrier due to high gravimetric energy density and low environmental impact. The hydrogen-evolution reaction (HER) by electrolysis of water to generate hydrogen from renewable energies provides a sustainable resource [1]. Successful adoption of the hydrogen energy cycle requires cost-efficient, environmentally benign, and sustainable catalysts. The current state-of-the-art HER catalysts use platinum (Pt), which is too expensive and scarce to be compatible with industrialization [2]. To overcome this limitation, research is being conducted to develop catalysts that do not use noble metals. Among them, transition metal carbide, phosphide, and sulfide show good HER performance [3-6]. However, metal phosphide has a limit for controlling intrinsic activity through the phase control (e.g., the content of P), since the electrochemical conductivity and chemical stability is greatly affected by the P content [5,7]. Transition metal sulfides (e.g., $MoS_2$, $WS_2$) have intrinsically low electrical conductivity and limited density of active sites only at the edge [8,9]. On the other hand, transition metal carbides (TMCs) have no penalty for controlling phase (C content), and no restriction of active sites position. Furthermore, TMCs have the advantages of low price, abundant reserves, physical safety, high electrical conductivity, wide pH applicability, and Pt-like activity [10-12]. The representative TMC electrocatalysts reviewed in this paper are summarized in Table 1.

In early TMCs (e.g., molybdenum carbide, tungsten carbide), a carbon atom placed at the interstitial site of a transition metal (TM) induced mixing and rehybridization between the s-p orbitals of C, and the d orbitals of the TM [10,11,13]. Consequently, d-band electronic density of states at the Fermi level $E_F$ resembles that of Pt and yields Pt-like catalytic activity [13,14]. TMCs have been evaluated for use in numerous reactions, including water-gas shift [15], hydrogenation [16], and desulfurization [17]. TMC also showed promising results in harsh conditions of HER [12].

This review provides an overview of how TMCs have been developed and used as HER catalysts. Molybdenum carbide and tungsten carbide are considered in-depth because they are the most-studied and most-promising materials [18]. The two main approaches to increase the catalytic activity of TMC have been to increase the number of active sites and to increase the intrinsic activity of the carbide. These two approaches have been exploited in development strategies, including nanostructuring using inorganic-organic complex, utilizing as-made carbon support, doping with heteroatoms, and engineering of heterostructures and phase. We close by considering future development and challenges of TMC HER catalyst.

## KINETICS AND THERMODYNAMICS OF HER

The kinetics of HER vary with pH of an electrolyte (Fig. 1(a)) [19]. In acidic aqueous media, the first step of HER is the Volmer Step, which is reduction of a proton at the active site of the catalyst:

†To whom correspondence should be addressed.
E-mail: jwlee1@kaist.ac.kr
‡These authors contributed equally.

**Table 1. Summary of HER performance of TMC catalysts reviewed here**

| Electrolyte | Catalyst | Loading (mg $cm^{-2}$) | Overpotential at 10 mA $cm^{-2}$ (mV) | Tafel slope (mV $dec^{-1}$) | Ref. |
|---|---|---|---|---|---|
| 0.5 M $H_2SO_4$ | MoC-$Mo_2C$ nanowires | 0.14 | 126 | 43 | 41 |
| | $Mo_2C$@NC | 0.28 | 124 | 60 | 63 |
| | $Mo_2C$@carbon | 0.25 | 78 | 41 | 40 |
| | $MoC_x$ octahedrons | 0.80 | 142 | 53 | 68 |
| | MoCN-3D | 0.26 | 87 | 51.4 | 69 |
| | $Mo_2C$@NPC/NPRGO | 0.14 | 34 | 33.6 | 44 |
| | $Mo_2C$/CNT-GR | 0.65-0.67 | 130 | 58 | 71 |
| | Ni-$Mo_2$ C@C | 0.531 | 72 | 65.8 | 47 |
| | P-$Mo_2C$@C | 1.30 | 89 | 42 | 73 |
| | N@MoPCx-800 | 0.14 | 108 | 69.4 | 62 |
| | v$Mo_xC$ | 1.00 | 130 | 60.4 | 42 |
| | $W_2C$/MWNT | 0.56 | 123 | 45 | 58 |
| | WC@NPC | 0.209 | 51 | 49 | 83 |
| | P-$W_2C$@NC | 3.50 | 89 | 53 | 84 |
| | WC nanowalls | - | 160 | 67 | 85 |
| | p-$WC_x$ NWs | 1.08 | 118 | 55 | 86 |
| | $Fe_3C$@NCNT | 0.765 | 154 | 97 | 94 |
| | $V_8C_7$@GC NSs/NF | 1.90 | 47 | 44 | 95 |
| 1.0 M $HClO_4$ | $Mo_2C$-$MoO_x$/CC | 1.7-1.9 | 60 | 53 | 56 |
| 1.0 M KOH | MoC-$Mo_2C$ | 0.14 | 120 | 42 | 41 |
| | $Mo_2C$@NC | 0.28 | 60 | - | 63 |
| | $MoC_x$ octahedrons | 0.80 | 151 | 59 | 68 |
| | MoCN-3D | 0.26 | 122 | 78.4 | 69 |
| | N,P-doped $Mo_2C$@C | 0.90 | 47 | 71 | 49 |
| | v$Mo_xC$ | 1.00 | 116 | 69 | 42 |
| | P-$W_2C$@NC | 3.50 | 63 | 65 | 84 |
| | p-$WC_x$ NWs | 1.08 | 122 | 56 | 86 |
| | $V_8C_7$@GC NSs/NF | 1.90 | 38 | 34.5 | 95 |
| 0.1 M KOH | $Co_2C$ NPs | 0.707 | 181 | 89 | 93 |

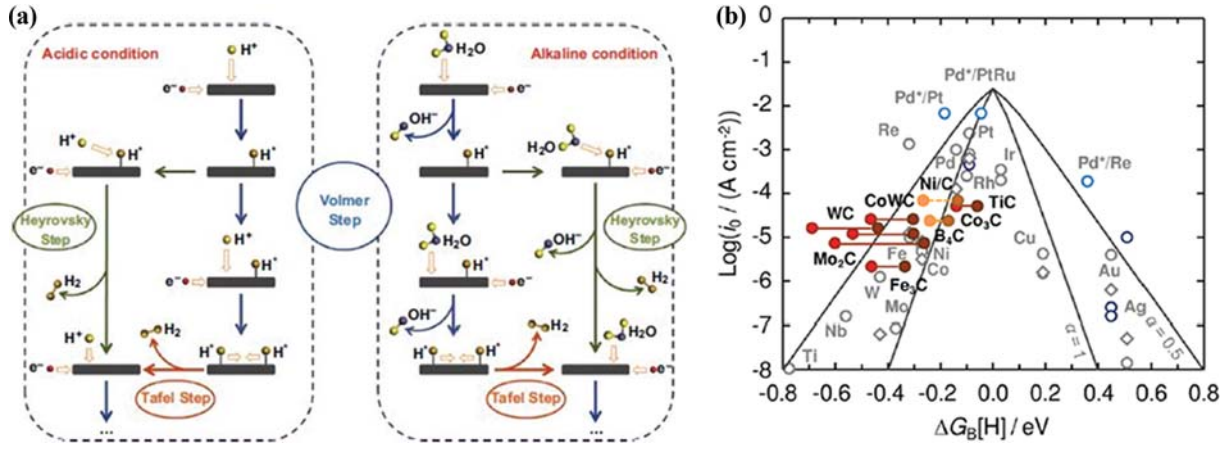


**Fig. 1. (a) Schematic illustrations of HER mechanisms in acidic and alkaline media (Reproduced with permission from Ref. [3], Copyright 2018, Springer Nature). (b) Volcano relationships of exchange current density and hydrogen binding energy of various HER electrocatalysts (Reproduced with permission from Ref. [23], Copyright 2014, American Chemical Society).**

$$H^+_{(aq)} + e^- \rightarrow H_{ads} \quad (1)$$

The next step is either the Heyrovsky Step, which is electrochemical desorption,

$$H_{ads} + H^+_{(aq)} + e^- \rightarrow H_{2(g)} \quad (2)$$

or the Tafel step, which is chemical recombination:

$$H_{ads}+H_{ads}\rightarrow H_{2(g)} \quad (3)$$

In alkaline aqueous media the HER also proceeds by either the Vomer-Heyrovsky (4), (5) or Volmer-Tafel (4), (6) mechanism:

$$H_2O+e^-\rightarrow H_{ads}+OH^- \quad (4)$$

$$H_2O+H_{ads}+e^-\rightarrow H_{2(g)}+OH^- \quad (5)$$

$$H_{ads}+H_{ads}+e^-\rightarrow H_{2(g)} \quad (6)$$

In alkaline media, the Volmer step entails adsorption of a water molecule followed by its dissociation into a proton and a hydroxide ion. This step entails cleaving an H-O bond; this action has a very high energy barrier, so this step is generally considered to be the rate-determining step of alkaline HER. When Pt is used as the catalyst, the reaction rate is two or three orders of magnitude slower than in acid media [20].

Tafel slope (slope of a plot of $\log_{10}$(current density) on overpotential $\eta_{10}$ to reach 10 mA $cm^{-2}$, which is the expected current density of a 12.3%-efficient solar cell [21]) is an indicator of kinetics. The Tafel slopes of the Volmer, Heyrovsky and Tafel steps are 118, 39, and 29 mV $dec^{-1}$ respectively [22], so the rate-determining step can be deduced (e.g., it is the Volmer step if the Tafel slope is ~120 mV $dec^{-1}$).

The Gibbs free energy $\Delta G_{H^*}$ of hydrogen binding is a thermodynamic indicator. It represents the interaction between hydrogen and the catalyst's active site. $\Delta G_{H^*}>0$ means hydrogen binding is weak, and hydrogen adsorption is slow (Volmer step). Conversely, $\Delta G_{H^*}<0$ means that hydrogen binding strong; as a result, hydrogen desorption (Heyrovsky or Tafel step) is slow, and undetached hydrogen blocks the active sites, so the reaction is slow. As far as known, the most effective HER catalyst is Pt or a Pt-group metal (PGM) (Fig. 1(b)) [23]. These catalysts have $\Delta G_H$ that is close to the ideal value, zero.

## MOLYBDENUM CARBIDE

Molybdenum carbide has high conductivity, and an electronic configuration similar to that of Pt [10,13]. Excellent HER activity and stability in both acidic and basic conditions of commercial

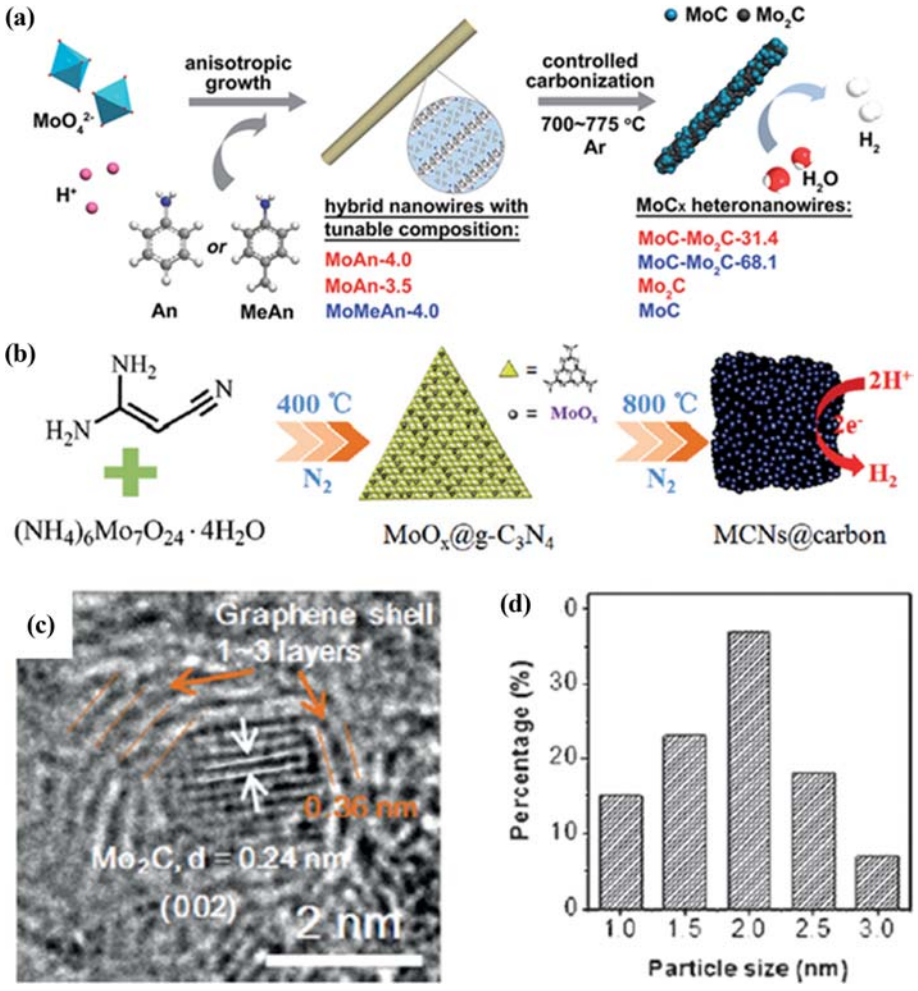


**Fig. 2. Nanostructuring using Inorganic-organic complex. (a) Schematic of $Mo_xC$ NWs fabrication from $MoO_x$-amine hybrid NWs (Reproduced with permission from Ref. [41], Copyright 2016, The Royal Society of Chemistry). (b) Synthesis schematic, (c) HRTEM image, and (d) particle-size distribution of $Mo_2C$ NPs (Reproduced with permission from Ref. [40], Copyright 2015, Wiley-VCH).**

$Mo_2C$ was first reported in 2012 [12]. However, use of molybdenum carbide to replace Pt has encountered two main impediments. First, conventional gas phase carburization or temperature programmed reduction (TPR) are not ideal for nanostructuring. The chemical reduction of metal precursors to carbide requires temperature >700 °C and highly-flammable hydrocarbon gases (e.g., $CH_4$, $C_2H_6$, CO), and the reaction surfaces are vulnerable to coking, particle sintering and collapse of nanostructure, all of which significantly reduce number of active sites [24-31]. Gas composition also affects factors such as phases, surface area, and coking [32]. Various phases of TMC show different catalytic activities [33-35]. Thus, TMC should be engineered to have the most active phase and high surface area. Chemical vapor deposition (CVD) can be used to fabricate TMCs, but this method also uses hazardous precursors and can result in chars [36-38]. It also requires expensive equipment, high vacuum, and relatively complex manipulation. The resultant catalysts also have insufficient intrinsic activity to replace PGMs. Although TMC has weaker hydrogen-binding energy than do pure TMs (i.e., lower d-band center than that of TM), it is still stronger that the ideal binding strength (Fig. 1(b)) [13]. The major development strategies have been efforts to solve these problems. To avoid particle sintering and coking, methods that use inorganic-organic complexes [39-42] and carbon supports [43-45] have been introduced. To compensate for low catalytic activity, the d-band center has been tuned by heteroatom doping [46-50], novel heterostructure [51-56] has been designed and phases [57-59] of TMC have been controlled.

**1. Nanostructuring using Inorganic-organic Complex**

Despite their Pt-like electronic configuration, initial molybdenum carbide catalysts have far inferior HER catalytic activity to that of commercial Pt/C catalyst. However, in recent years, TMC HER catalysts have improved dramatically by preventing particle aggregation during heat treatment. N-rich precursors (e.g., urea, dicyandiamide, melamine) have been used to fabricate ultrafine TMC nanoparticles (NPs) [40,42,60]. Inorganic-organic complexes provide diverse novel carburization methods [61]. Organic domains provide carbon during heat treatment [62], so the hazardous conventional hydrocarbon precursors can be replaced. Carburization by solid-solid diffusion of carbon provides much more defined nanostructure than traditional gas-solid diffusion [14,27]. Inorganic domains can promote dispersion of TM by retaining nanostructure [42].

Heteronanowires (HNWs) of MoC-$Mo_2C$ have been synthesized by controlled carbonization of $MoO_x$-amine (amine=aniline or *p*-methylaniline) (Fig. 2(a)) [41]. The MoC ratio is increased by choosing a precursor that has high carbon content (*p*-methylaniline) and by decreasing the carbonization temperature. $Mo^{3+}/Mo^{2+}$ mole ratios analyzed by XPS effectively tell the electron density on Mo sites. In 0.5 M $H_2SO_4$ and 1.0 M KOH, the optimal MoC-$Mo_2C$ (31.4 wt% MoC) had low $\eta_{10}$ (126 and 120 mV), respectively, and small Tafel slope (43 and 42 mV decade$^{-1}$), respectively.

Ultrasmall molybdenum carbide embedded within nitrogen-rich carbon ($Mo_2C$@NC) can be synthesized simply by mixing ammonium molybdate and dicyandiamide, then heating to 800 °C under Ar flow [63]. Dicyandiamide has the critical function of promot-

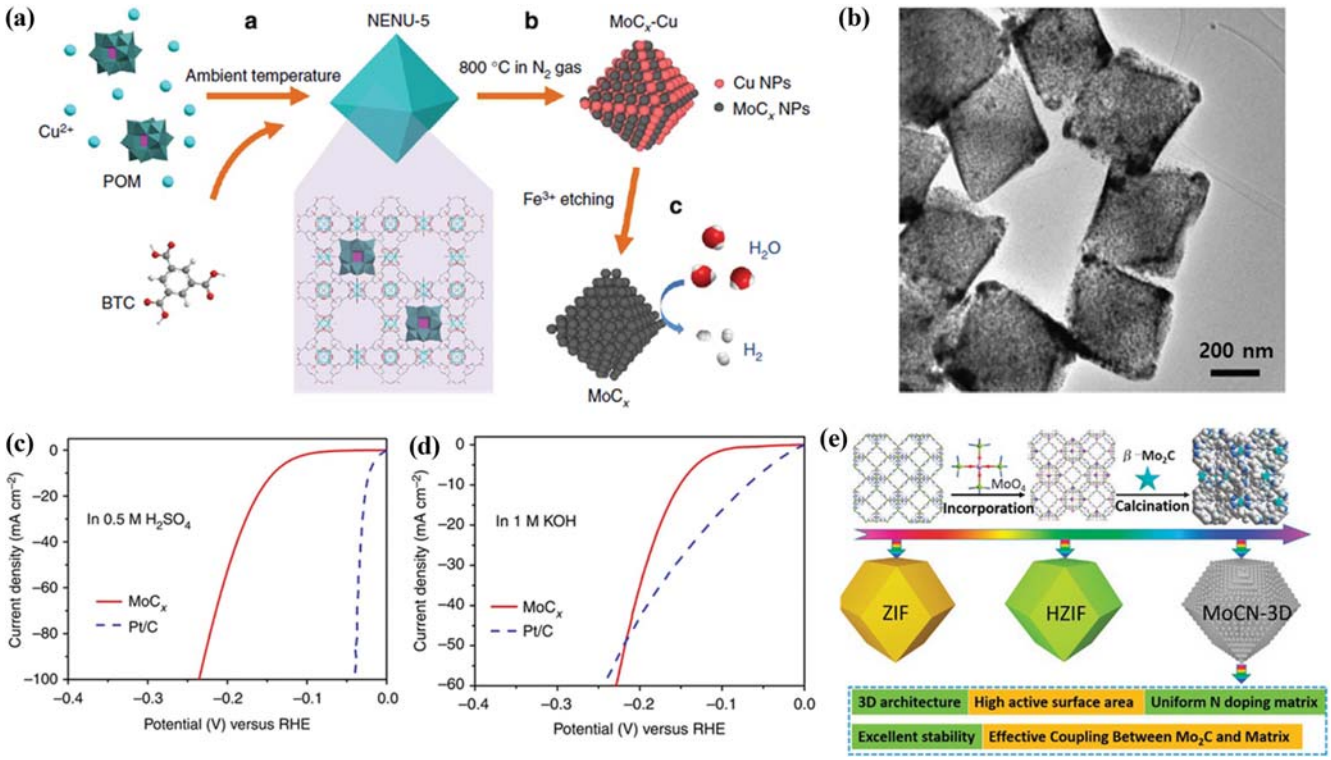


**Fig. 3. (a) Schematic of the synthesis procedure, (b) TEM image, and polarization curves of $MoC_x$ nano-octahedrons in (c) 0.5 M $H_2SO_4$ and (d) 1.0 M KOH (Reproduced with permission from Ref. [68], Copyright 2015, Springer Nature). (e) Schematic of the synthesis procedure of HZIF-Mo-derived compound MoCN-3D (Reproduced with permission from Ref. [69], Copyright 2016, Springer Nature).**

ing ammonium molybdate reduction and *in-situ* generation of nitrogen-rich carbon compounds. $Mo_2C$@NC showed outstanding HER activity in a wide pH range; $\eta_{10}$ was 124, 156 and 60 mV in acidic, neutral and basic media, respectively.

Ultrafine $Mo_2C$ embedded in graphitic carbon nitride (g-$C_3N_4$) was fabricated [40] using the same precursors as in [63]. First, $MoO_x$ was fabricated in g-$C_3N_4$ by dicyanamide condensation at 400 °C, then oxide was converted to $Mo_2C$ NP at 800 °C (Fig. 2(b)). The optimized $Mo_2C$ NPs were naturally encapsulated by 1-3 layers of ultrathin graphene shells (Fig. 2(c)), which efficiently prevented aggregation at high temperature and reduced electrical resistance between adjacent nanoparticles. The confining effect of g-$C_3N_4$ also prohibits particle aggregation and promotes high dispersion of $Mo_2C$ NPs and formation of small (<3 nm) $Mo_2C$ NPs (Fig. 2(d)). As-made $Mo_2C$ NPs showed excellent activity of $\eta_{10}$=78 mV, and a Tafel slope of 41 mV decade$^{-1}$ in 0.5 M $H_2SO_4$. The number of active sites naturally increased along with formation of highly dispersed, uniform, and ultrafine particles. Therefore, the activity of TMC was greatly increased, and maximized the usage of limited catalyst.

Metal-organic frameworks (MOFs) can also prevent particle agglomeration. MOFs are constructed by chemical bonding between metal ions and organic ligands [64,65]. Tunable chemical composition and crystalline structure of MOF have advantages as both a precursor and a template. MOFs are great templates because of their porous structure and high density of active sites [66,67]. Also, the organic ligand can work as a carbon precursor.

$MoC_x$ nano-octahedrons have been synthesized using an MOF-assisted strategy [68]. First, the largest pores of Cu-based MOF [HKUST-1; $Cu_3(BTC)_2(H_2O)_3$] are periodically filled with Mo-based Keggin-type polyoxometalates ($H_3PMo_{12}O_{40}$) to make $[Cu_2(BTC)_{4/3}(H_2O)_2]_6[H_3PMo_{12}O_{40}]$ (NENU-5; $BTC_{1/4}$=benzene-1,3,5-tricarboxylate). Then, NENU-5 nano-octahedrons are heated at 800 °C under $N_2$ flow, then etched using $Fe^{3+}$ to remove metallic Cu NPs (Fig. 3(a)). As a result, *in-situ* $Mo_xC$ nanocrystallites are generated by a reaction with polyoxometalates and carbonaceous species that were derived from the BTC ligands. This confined carburization reaction between organic ligand and guest metal source prevents agglomeration and coalescence during heat treatment by isolating the metal source inside the carbon framework from decomposition of the MOF. As-made ultrafine $MoC_x$ nanocrystallites were mostly of size <5 nm, so they had high specific surface areas and consequent high catalytic activity in both 0.5 M $H_2SO_4$ ($\eta_{10}$=142, Tafel slope=53 mV decade$^{-1}$) and 1.0 M KOH ($\eta_{10}$=151 mV, Tafel slope=59 mV decade$^{-1}$) (Fig. 3(b)-(d)).

Similarly, bimetallic MOF has been converted directly to a composite of ultrafine $Mo_xC$ NPs (<5 nm) and nitrogen-doped carbon matrix [69]. When molybdic acid is mixed with zeolitic imidazolate framework (ZIF, a type of MOF), some $Zn(im)_4^{2-}$ units in ZIF-8 are replaced by $MoO_4^{2-}$ (Fig. 3(e)). As-made hybrid zeolite imidazolate framework (HZIF) was pyrolyzed at 700 °C under Ar flow, then treated with acid to remove unevaporated zinc. The resulting $Mo_xC$ embedded in N-implanted 3D carbon matrix (MoCN-3D) showed a low $\eta_{10}$=87 and small Tafel slope=51.4 mV dec$^{-1}$ in 0.5 M $H_2SO_4$, and $\eta_{10}$=122 mV and a Tafel slope=78.4 mV dec$^{-1}$ in 1.0 M KOH. Hierarchical pore structure and ultrafine $Mo_xC$ NPs account for the excellent activity in both acid and alkaline media.

## 2. Carbon Supports

Various carbon-based supports such as carbon nanotube (CNT)

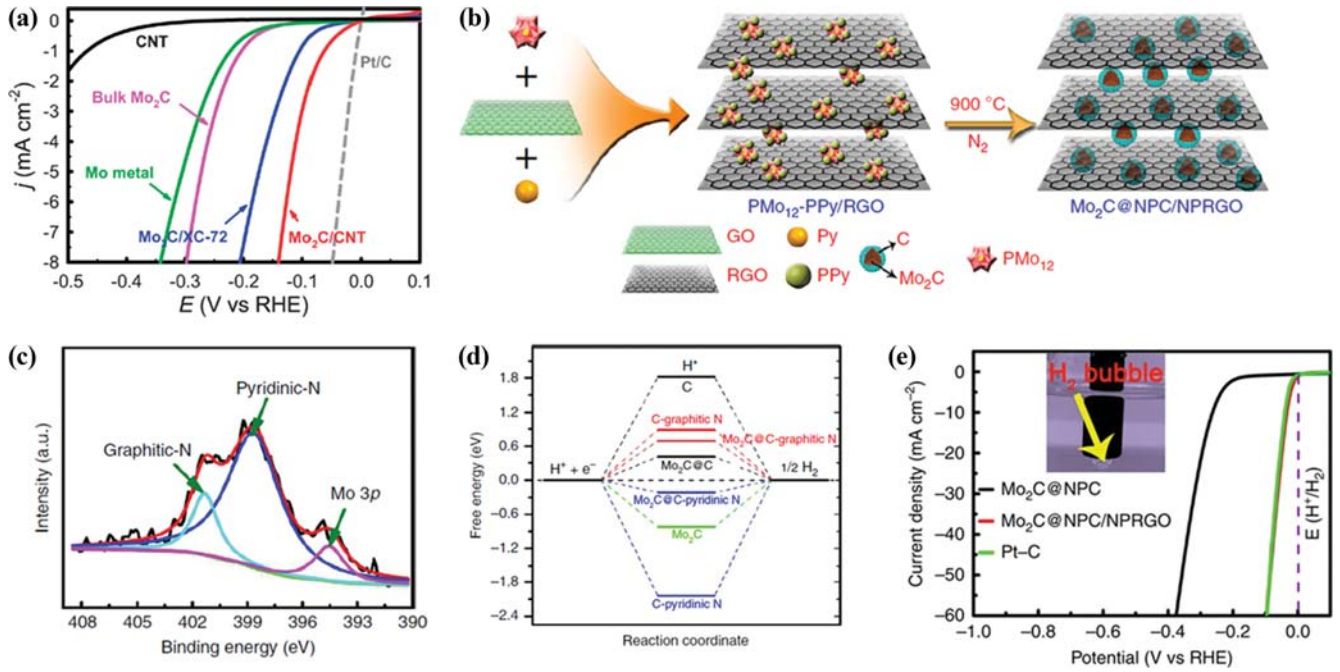


**Fig. 4. Utilization of carbon supports. (a) HER polarization curves of $Mo_2C$/CNT, $Mo_2C$/XC-72, Mo metal, and bulk $Mo_2C$ in $H_2$-purged 0.1 M $HClO_4$ (Reproduced with permission from Ref. [27], Copyright 2013, The Royal Society of Chemistry). (b) Schematic of the synthesis procedure (c) XPS N 1s high-resolution scan, (d) HER polarization curve (in 0.5 M $H_2SO_4$) of $Mo_2C$@NPC/NPRGO. (e) DFT-calculated HER activities for various systems (Reproduced with permission from Ref. [44], Copyright 2016, Springer Nature).**

[43], reduced graphene oxide (RGO) [44], and carbon-fiber paper [45], are used for nanostructuring and electronic modification. A well-defined carbon matrix can increase the number of active sites by increasing particle dispersity, can increase electrical conductivity, and can stimulate HER activity by modification of electrochemical structure.

Carbon supports affect the catalytic activity of $\beta$-$Mo_2C$ nanoparticles on CNT ($Mo_2C$/CNT) and XC-72R carbon black ($Mo_2C$/XC) [27]. Ammonium molybdate was mixed with carbon support, then annealed at 800 °C under Ar flow. $Mo_2C$ NPs on carbon supports were evenly distributed with an average diameter of 12 nm. In 0.1 M $HClO_4$, the catalytic activity was superior in the order $Mo_2C$/CNT> $Mo_2C$/XC>$Mo_2C$ (Fig. 4(a)). Three main synergetic effects between $Mo_2C$ NP and carbon support account for increased activity. First, covalent $Mo_2C$-CNT binding structure provide a physical barrier, which prevents aggregated growth of $Mo_2C$ NP. Second, a ligand effect [70] from the Mo-C bonding (i.e., charge transfer from Mo to C) downshifts the d-band center of Mo, and thereby shifts Mo-H binding strength toward optimal. Third, covalent conjugation provides a resistance-less path for fast electron transfer, so kinetics is accelerated.

Coupling of RGO with molybdenum carbide has a synergetic effect on catalytic activity, in the form of a carbonized ternary $PMo_{12}$-PPy/RGO nanocomposite ($PMo_{12}=H_3PMo_{12}O_{40}$, PPy=polypyrrole) (Fig. 4(b)) [44]. As-synthesized $Mo_2C$ NPs (≈2-5 nm) are encapsulated by N,P-codoped carbon shells and embedded on N,P-codoped 2D RGO ($Mo_2C$@NPC/NPRGO). During the annealing process, the RGO prevents aggregation of Mo compounds, so they maintain high dispersion and numerous active sites. Carbon shells also hamper particle sintering and promote electron transfer. N-doping of carbon matrix was mainly by pyridinic-N (Fig. 4(c)). Density functional theory (DFT) calculations support the experimental data of synergetic effect between $Mo_2C$ NP and N-doped RGO (favorable $\Delta G_{H^*}=-0.22$ eV) (Fig. 4(d)). As a result, $Mo_2C$@NPC/NPRGO has an extremely low $\eta_{10}$ of 34 mV and a remarkably small Tafel slope of 33.6 mV $dec^{-1}$ in 0.5 M $H_2SO_4$ (Fig. 4(e)).

$Mo_2C$ NP on CNT-graphene support ($Mo_2C$/CNT-GR) was developed [71] by heating a metal-urea complex on CNT-GO under $N_2$ atmosphere at 750 °C. CNT-GR hybrid alleviates aggregation and facilitates electron transfer. This general synthesis method can be applied to produce $Mo_2N$ by decreasing the urea/metal molar ratio, or to produce $MoS_2$ by replacing urea with thiourea. Thus, HER activity of $Mo_2C$, $Mo_2N$ and $MoS_2$ can be rationally compared; $Mo_2C$ shows the lowest $\eta_{10}$=130 mV among them ($Mo_2N$/CNT-GR: $\eta_{10}$=186 mV; $MoS_2$/CNT-GR: $\eta_{10}$=255 mV) in 0.5 M $H_2SO_4$.

### 3. Heteroatom Doping

Doping with heteroatoms can adjust intrinsic catalytic activity of Mo by modifying its electronic structure [47,72]. Although the d-band electron structure of molybdenum carbide is similar to that of Pt, Mo has fundamentally limited activity because the empty d-orbitals cause strong hydrogen binding that slows hydrogen desorption. Late TMs have electron-rich d-orbitals. Doping these metals into TMC can downshift the d-band center with respect to $E_F$, and this change improves the HER kinetics.

A systematic study showed the effect of TM doping on the HER catalytic efficiency of $Mo_2C$ [47]. Pyrolysis of $(NH_4)_n[TMMo_6O_{24}H_6]\cdot$

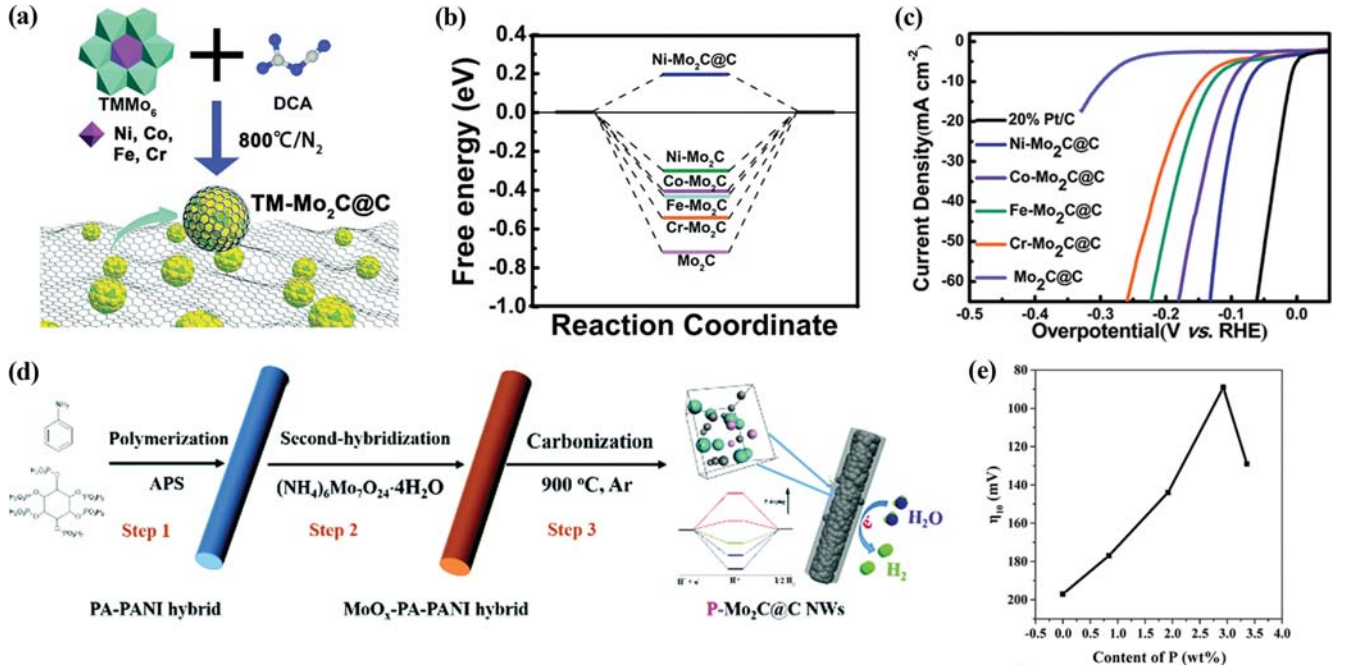


**Fig. 5. (a) Schematic of the synthesis, (b) HER polarization curves (in 0.5 M $H_2SO_4$), and (c) calculated free-energy diagram for HER of various TM-catalysts. TM-$Mo_2C$@C means TM-$Mo_2C$ covered by N-doped carbon (Reproduced with permission from Ref. [47], Copyright 2018, The Royal Society of Chemistry). (d) Schematic of synthesis and structure of P-$Mo_2C$@C NWs and (e) HER $\eta_{10}$ required of P-$Mo_2C$@C in 0.5 M $H_2SO_4$ with content of P (Reproduced with permission from Ref. [73], Copyright 2017, The Royal Society of Chemistry).**

$5H_2O$ (TM=$Ni^{2+}$, $Co^{2+}$, n=4; TM=$Fe^{3+}$, $Cr^{3+}$, n=3) and dicyandiamide powder at 800 °C (Fig. 5(a)) yielded TM-doped $Mo_2C$ nanoparticles that were covered with few-layer N-doped graphitic carbon shells (TM-$Mo_2C$@C). Systematic investigation on effects of TM doping was possible because ratio of dopant to Mo, particle size and catalyst morphology did not vary with various TM. DFT indicated that the relatively strong hydrogen interaction of pure $Mo_2C$ is weakened by doping with TMs. In the order Ni-$Mo_2C$>Co-$Mo_2C$>Fe-$Mo_2C$>Cr-$Mo_2C$>$Mo_2C$, $\Delta G_{H^*}$ approaches the ideal value (Fig. 5(b)). When the DFT calculation model includes an N-doped carbon shell, $\Delta G_{H^*}$ approaches zero even more closely and the experimental results match theory calculation. When $Mo_2C$ was doped with TM, both activity and Tafel slope improved compared to that of pure $Mo_2C$. In in 0.5M $H_2SO_4$ Ni-$Mo_2C$@C, which has the most enhanced activity, has low $\eta_{10}$=72 mV, and a Tafel slope of 65.8 mV $dec^{-1}$ (Fig. 5(c)). However, to optimize HER, only a moderate amount of TM dopant should be applied, as too much degrades the HER activity. Similarly, doping with Fe changes the lattice parameters and valence state of $Mo_xC$ [48]. At some point, the increasing Fe atomic percentage changes the phase of the molybdenum carbide from $\beta$-$Mo_2C$ to $\gamma$-MoC, so the HER activity decreases with excess Fe doping.

Non-metallic dopants (e.g., N [45], P [73], S [74]) that have different electronegativity than carbon are alternative options. P-doping into $Mo_2C$ (0-3.4 wt%) can be tuned by carbonizing $MoO_x$-phytic acid-polyaniline ($MoO_x$-PA-PANI) hybrid (Fig. 5(d)) [73]. As-made P-doped $Mo_2C$ nanoparticles are evenly embedded in hierarchical carbon nanowires (P-$Mo_2C$@C). P-doping percentage varies with the amount of phytic acid added. Phosphorus (2.19) has lower electronegativity than carbon (2.55), sulfur (2.58) and nitrogen (3.04). Thus, P-doping can effectively downshift the density of the empty d-band in $Mo_2C$; this process is filling of anti-bonding orbital [54,75] and results in weakened H-binding strength of $Mo_2C$. Distribution of P on the surface contributes to weakening the H-binding by inducing steric hindrance around active sites ($Mo^{2+}$). DFT calculation showed that increased P doping weakens H bonding ($\Delta G_{H^*}$~0) until the optimum point (2.9 wt%); this result agrees well with experimental result (Fig. 5(e)). Further doping leads to positive $\Delta G_{H^*}$, so HER kinetics is reduced due to insufficient strength for $H^+$ reduction in the first step. In 0.5 M $H_2SO_4$, P-$Mo_2C$@C achieved a low $\eta_{10}$=89 mV and a small Tafel slop of 42 mV $dec^{-1}$.

N,P-doped $Mo_2C$@C [49] also showed increased HER catalysis. Phosphomolybdic acid ($H_3PMo_{12}O_{40}\cdot nH_2O$, $PMo_{12}$) was used to initiate the polymerization of pyrrole (PPy). Polymeric nanosphere was synthesized stirring $PMo_{12}$ and Py at room temperature, then subjected to carbothermal reduction at 800 °C under Ar flow. As-made catalyst (S-800) is composed of $Mo_2C$ nanoparticles encapsulated in graphitic carbon shells. In 1.0 M KOH, the N, P co-doped S-800 showed superior $\eta_{10}$=47 mV. A synergistic coupling effect between N and P accounts for the improved activity.

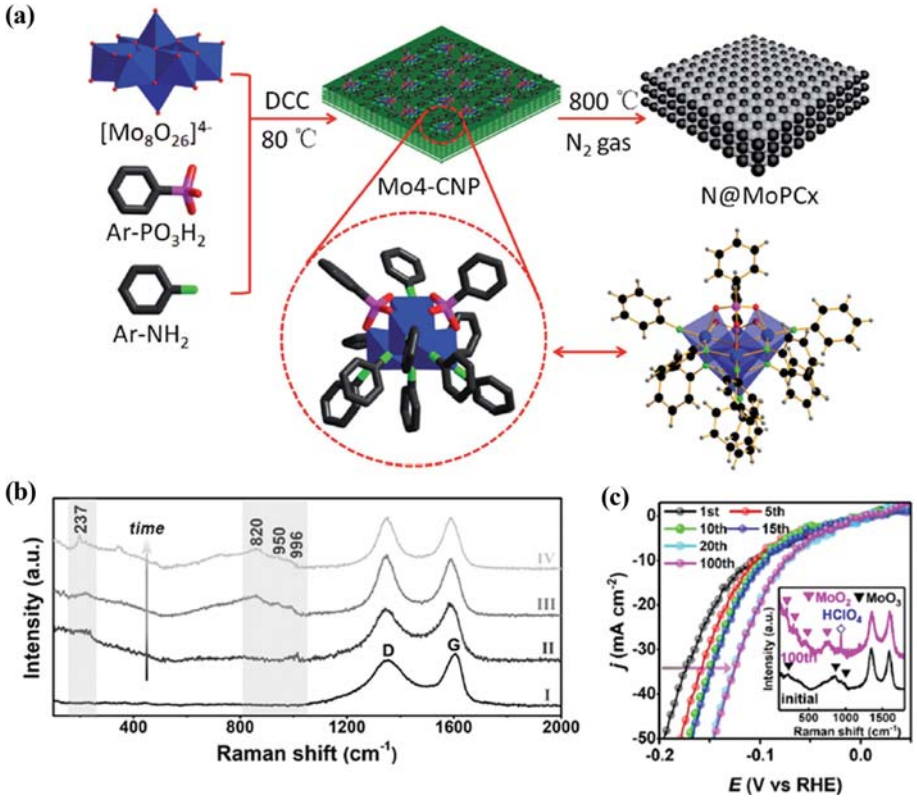


**Fig. 6. (a) Schematic of synthesis procedure of porous N-doped molybdenum carbide and phosphide hybrid (Reproduced with permission from Ref. [62], Copyright 2018, Wiley-VCH). (b) Raman spectra of $Mo_2C$/CC and $Mo_2C$-$MoO_x$/CC after surface oxidation for various times. (c) HER polarization curves (in 1.0 M $HClO_4$) of $Mo_2C$-$MoO_x$/CC(2) (Reproduced with permission from Ref. [56], Copyright 2020, Wiley-VCH).**

N,P-co-doped graphene showed better HER activity than either N or P single-doped graphene [76].

**4. Heterostructure and Phase Control**

Heterostructures are composed of two or more electrochemically active materials [77]. Heterostructures can have synergetic effects as a result of modification of electronic state and transfer of electrons at heterogeneous interfaces [78]. Many studies of molybdenum carbide in heterostructures showed superior HER activity due to synergistic effects on interfaces (e.g., MoP-MoC, $MoO_2$-$Mo_2C$, $Mo_2C$-$Mo_2N$, $MoS_x$@$Mo_2C$) [52,53,79,80].

N-doped Mo carbide-phosphide hybrid nanosheets (N@MoPCx) show a synergy [62]. $Mo_4O(ArPO_3)_2(NAr)_4(\mu_2\text{-}NAr)_5$ (Ar=phenyl, Mo4-CNP) is a precursor in which aniline is partially replaced by phenylphosphonic acid; the precursor is subjected to confined carburization and phosphorization simultaneously (Fig. 6(a)). In 0.5 M $H_2SO_4$, as-prepared porous N@MoPCx showed a $\eta_{10}$=108 mV and a small Tafel slope=69.4 mV $dec^{-1}$, which are both better than N-doped $Mo_2C$ and MoP, separately.

Heterostructured $Mo_2C$-$MoO_x$ has been achieved on carbon cloth ($Mo_2C$-$MoO_x$/CC) by oxygen plasma treatment [56]. *In situ* reduction of $Mo^{VI}$ oxides to $Mo^{IV}$ significantly promoted HER activity (Fig. 6(b)-(c)). DFT calculations indicate that terminal Mo=O moieties has a critical function in moving negative the $\Delta G_{H^*}$ of $Mo_2C$ to close to zero, and thereby promoting H* desorption. In 1.0 M $HClO_4$, the optimized $Mo_2C$-MoOx/CC had a superior $\eta_{10}$=60 mV, whereas $Mo_2C$/CC has $\eta_{10}$=153 mV.

Molybdenum carbide has four representative phases: $\alpha$-$MoC_{1-x}$, $\beta$-$Mo_2C$, $\gamma$-MoC, $\eta$-MoC. The electrocatalytic activity generally varies greatly depending on the atomic ratio of Mo to C. When the crystal structure is changed, the surface distributions of Mo and C change, so the catalytic properties also change. The degree of packing also differs, so degree of ion insertion changes. For example, $\alpha$-$MoC_{1-x}$ has FCC structure, whereas the others have similar hexagonal crystal structures with different stacking sequences. Thus, the phases of molybdenum carbide have distinct HER activity and stability (Fig. 7) [33]. $\beta$-$Mo_2C$ and $\gamma$-MoC have good that originates from their Pt-like valence bands. Thus, regulating hetero-phases of molybdenum carbide can also elicit synergetic effect [42,57,81].

Highly-dispersed valence-controlled $Mo_xC$ on mesoporous carbon support (v$Mo_xC$) have been synthesized using interaction-mediator-assisted evaporation-induced self-assembly on a polymer (PEO-*b*-PS) template [42]. The valence state of Mo is tuned by the local environment (e.g., coordination state, nearby species, defects), which is adjusted by the air treatment temperature before carbonization at 1,100 °C. During phase transition, defective sites were generated at the grain boundary between $\alpha$-MoC to $\beta$-$Mo_2C$ accompanied by formation of additional active catalytic sites with moderate Mo-valence (Fig. 8(a)-(b)). Projected density of states (PDOS) showed that the phase transition alters the valence of Mo, and DFT calculations identify that active site with moderate Mo-valence leads to adequate hydrogen binding (Fig. 8(c)). Furthermore, volcano plots (Fig. 8(d)) with $Mo^{a+}/Mo^{b+}$ (0<a<1, 1<b<3) indicate that valence of Mo and intrinsic activity are greatly affected by the environment around Mo in both 0.5 M $H_2SO_4$ and 1.0 M KOH, the optimal v$Mo_xC$ had $\eta_{10}$ (130 and 116 mV) and Tafel slope (60.4 and 69.0 mV $dec^{-1}$). In 1.0 M KOH, the activity of v$Mo_xC$ exceeded that of Pt/C at 35 mA/$cm^2$.

## TUNGSTEN CARBIDE

Tungsten carbide also has Pt-like activity [82] with low cost and higher immunity to catalyst poisons (e.g., CO, $H_2S$) than Pt does. Tungsten carbide has characteristics similar to molybdenum carbide due to the characteristic metal-carbon bonding and has been developed in parallel ways. Two representative phases of tungsten carbide ($W_2C$, WC) have been extensively evaluated for use as an HER catalyst.

$W_2C$ has higher HER activity than WC [58]. Conventional carbide synthesis using hydrocarbon gases ($CH_4$, $C_2H_6$, or CO) cannot produce phase-pure $W_2C$, because the ratio of carbon to tungsten precursor is ungovernable, and carbon diffusion through the solid-gas interface is too fast. However, use of non-volatile crystalline solid-carbon precursor (i.e., multi-walled carbon nanotubes, MWNTs) allowed slow solid-solid carbon diffusion to $WO_x$. Carburization at 900 °C and 1,000-1,100 °C under Ar flow yields $W_2C$/MWNT and WC/MWNT, respectively. In 0.5 M $H_2SO_4$, $W_2C$/MWNT had

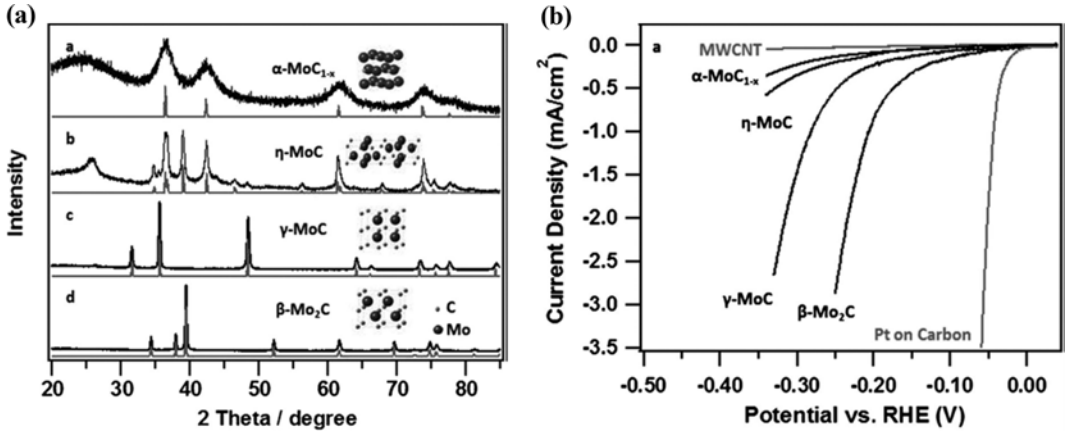


**Fig. 7. (a) XRD patterns and (b) HER polarization curves (in 0.1 M $HClO_4$) of four phases of Mo carbide (Reproduced with permission from Ref. [33], Copyright 2014, Wiley-VCH).**

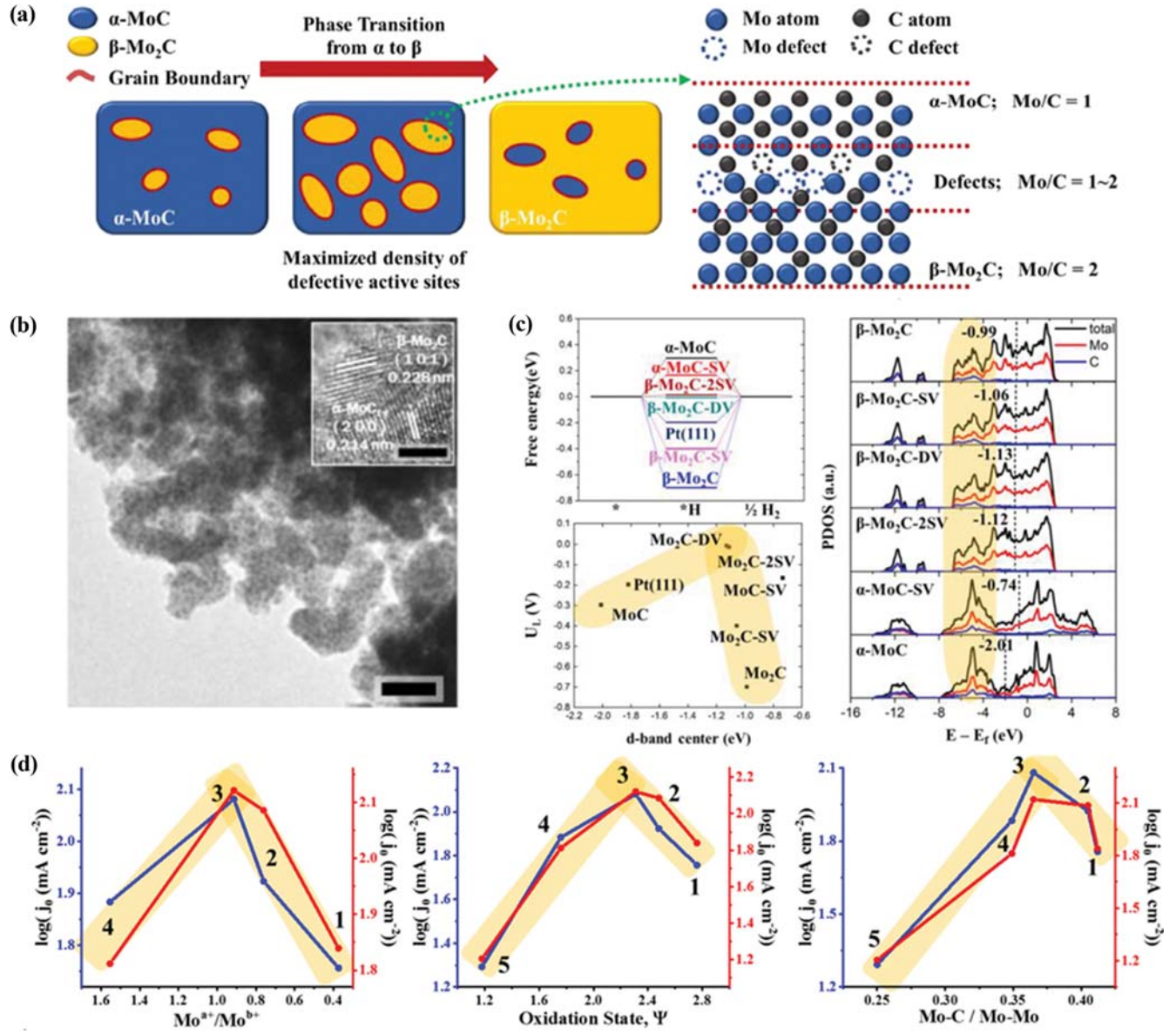


**Fig. 8. (a) Illustration of defective active site formation during phase transition. (b) TEM and HR-TEM (inset, scale bar, 2 nm) images, (c) free energy diagram of HER, relationships of d-band center and limiting potential $U_L$ of HER, and PDOS of $Mo_xC$ catalyst. (d) Volcano relationships of exchange current and valence state at −170 mV (vs. RHE) in acidic (red) and alkaline (blue) media (Reproduced with permission from Ref. [42], Copyright 2020, American Chemical Society).**

$\eta_{10}$=123 mV and a small Tafel slope of 45 mV $dec^{-1}$, which are superior to those of WC/MWNT. DFT calculation agreed well with the experimental results (Fig. 9). The high ratio of W in $W_2C$ raised its metallicity and the electronic density of states to near $E_F$, so electron transfer was facilitated. The MWNT support provided a physical barrier that confined the growth of tungsten carbide particles (size 2 to 5 nm). The support also has great conductivity, which accounts for the superior HER activity.

ZIF can induce cage-confinement pyrolysis and thus produce ultrasmall tungsten carbide particles [83]. $W(CO)_6$ (avg. diameter= 0.76 nm) is confined in thermal/chemical stable RHO-[$Zn(eim)_2$] (MAF-6, Heim=2-ethylimidazolate) that has hydrophobic nanocavities (diameter=1.84 nm) and flexible small apertures (avg. diameter=0.76 nm). High-temperature pyrolysis induces formation of highly dispersed WC nanoclusters/nanoparticles (≈2 nm) in nanoporous carbon (WC@NPC) (Fig. 10(a)-(b)). In 0.5 M $H_2SO_4$, WC@NPC had extremely low $\eta_{10}$=51 mV and Tafel slope of 49 mV $decade^{-1}$.

A N-doped carbon shell often covers nanoparticles during synthesis of carbide with dicyandiamide. For example, P-doped $W_2C$ can be encapsulated in an N-doped carbon shell (P-$W_2C$@NC) [84]. Annealing phosphotungstic acid ($H_3PW_{12}O_{40}{\cdot}xH_2O$, P source) and dicyandiamide (N source) at 400 °C under $N_2$ atmosphere produced well-dispersed $PW_{12}$ clusters isolated by $CN_x$ fragments. The $CN_x$ fragments allowed further confined carburization at 800 °C, then transformed to a multilayer N-doped carbon shell around

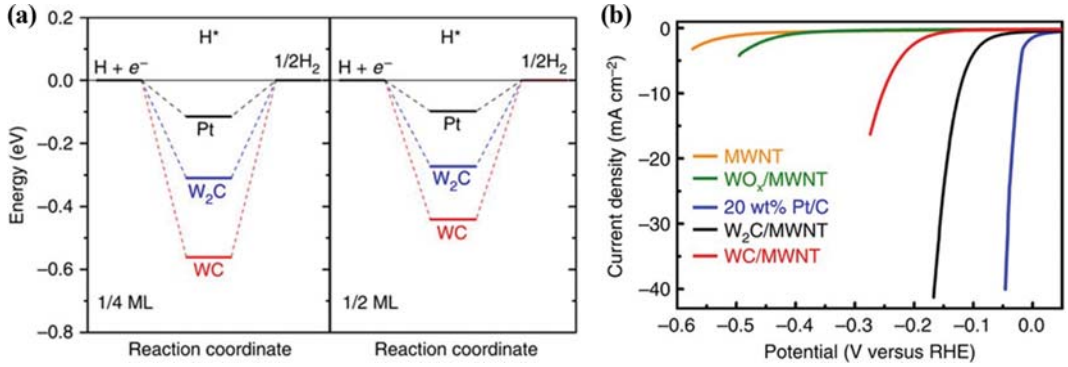


**Fig. 9. (a) Free-energy diagram of (0001) surfaces of tungsten carbides and (111) surface of Pt in HER. (b) HER polarization curves (in 0.5 M $H_2SO_4$) of $W_2C$/MWNT compared to WC/MWNT other control samples (Reproduced with permission from Ref. [14], Copyright 2016, Springer Nature).**

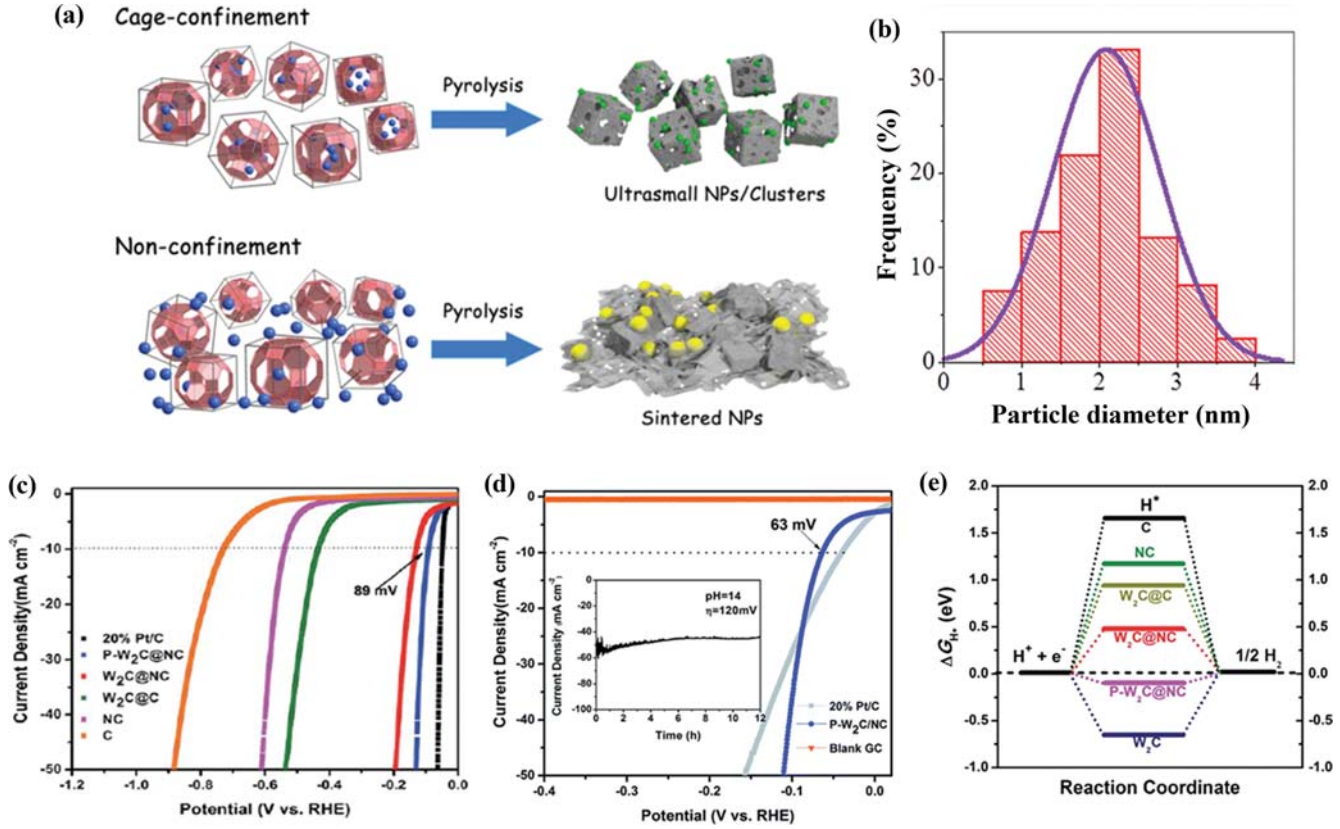


**Fig. 10. (a) Schematic comparing cage-confinement and non-confinement pyrolysis methods and (b) particle-size distribution of WC@NPC (Reproduced with permission from Ref. [83], Copyright 2017, American Chemical Society). HER polarization curves of P-$W_2C$@NC (c) in 0.5 M $H_2SO_4$ and (d) 1.0 M KOH. (e) Free-energy diagram of HER on various catalysts (Reproduced with permission from Ref. [84], Copyright 2017, The Royal Society of Chemistry)**

the $W_2C$ NPs. The N-doped carbon matrix can increase the stability, corrosion durability and electronic conductivity [47]. A coupling effect between carbide nanoparticle and N-implanted carbon positively modified electron density to near $E_F$ of the hybrid composite, so the $\Delta G_{H^*}$ was near zero [63]. In 0.5 M $H_2SO_4$, 1.0 M KOH and 0.1 M phosphate buffer, P-$W_2C$@NC had $\eta_{10}$=89, 63 and 185 mV, respectively (Fig. 10(c)-(d)). DFT calculations confirmed the effects of P-doping and the N-doped carbon shell; P-$W_2C$@NC gave $\Delta G_{H^*}$ value closer to zero than $W_2C$@NC did, and $W_2C$@C had $\Delta G_{H^*}$ farther from zero than $W_2C$@NC (Fig. 10(e)). DFT results agreed well with experimental results.

Modified CVD can also prepare tungsten carbide for efficient HER electrocatalysts. WC nanowalls can be grown by direct current plasma-assisted CVD (DC-PACVD) using pre-carburized tungsten cathode on Si wafer [85]. The WC nanowalls showed remarkable stability in 0.5 M $H_2SO_4$. No oxidation was observed for 10,000

cycles in the HER environment. In 0.5 M $H_2SO_4$, WC nanowalls had $\eta_{10}$=160 mV and a Tafel slop of 67 mV $dec^{-1}$. The extreme stability and activity of the nanowalls was attributed to the high crystallinity, smooth surface and nanoporous structure of pristine nanowalls.

Analogously, porous tungsten carbide hybrid nanowires (p-$WC_x$ NWs) have excellent HER activity [86]. $WO_x$ nanowires were grown on carbon cloth (CC) by placing CC on an alumina boat with $WO_3$ powder and heating. Then $WO_x$ NWs/CC was carbonized using a microwave plasma enhanced CVD (MPECVD). In 0.5 M $H_2SO_4$ and 1.0 M KOH, as-made p-$WC_x$ NWs had $\eta_{10}$ (118 and 122 mV) and a small Tafel slope (55 and 56 mV $decade^{-1}$), respectively. The superior HER activity originates from porous nano-structure and directional growth on CC. The CC facilitates electron transfer in the electrodes and eliminates the need for polymer binders and conducting agents, which might increase series resistance and block active sites [87].

## OTHER TRANSITION METAL CARBIDES

Titanium, chromium, iron, cobalt and nickel carbides have also been evaluated as HER electrocatalysts [36,88,89]. They have high potential as efficient HER electrocatalyst due to the unique physical and chemical properties, which originate from unusual metal-C bonding [38,90-92].

$Co_2C$ NPs with high electrocatalytic activity and stability have been synthesized using bromide-induced wet chemistry [93]. Dicobalt octacarbonyl, octadecylamine and cetrimonium bormide were heated at mild temperatures (up to 330 °C). In 0.1 M KOH, as-synthesized $Co_2C$ NPs had $\eta_{10}$=181 mV; their activity did not decrease even after 4,000 cycles in the HER environment. The high activity and stability were ascribed to the synergetic effect of Co-C and $Co(OH)_2$ at the surface.

$Fe_3C$ nanorods encapsulated in N-doped CNT ($Fe_3C$@NCNT) also show HER catalytic activity [94]. A mixture of $FeCl_3 \cdot 6H_2O$ and 1,4-dicarboxybenzene was dissolved in dimethylformamide (DMF) and NaOH then subjected to a hydrothermal treatment, followed by sequential addition of melamine and pyrolysis at 800 °C under $N_2$ flow. In 0.5 M $H_2SO_4$, $Fe_3C$@NCT had $\eta_{10}$=154 mV. DFT calculation ascribed the optimized hydrogen adsorption energy to a synergetic effect between iron carbide and N-doped CNTS.

Nanocrystalline $M_3C$ (M=Fe, Co, Ni) encapsulated in a graphitic shell and supported with vertically aligned graphene nanoribbons (VA-GNRs) were fabricated using a hot filament chemical vapor deposition (HF-CVD) technique. First, "teepee" structured VA-GNRs arrays were prepared on Si-wafer. Then the metals were deposited on the tips or side walls of VA-GNR, which were then carbonized by HF-CVD under gaseous carbon flow (Fig. 11(a)). In 0.5 M $H_2SO_4$ and overpotential of 200 mV, as-made $Fe_3C$-GNRs, $Co_3C$-GNRs, and $Ni_3C$-GNRs has large cathodic current density of 166.6, 79.6, and 116.4 mA $cm^{-2}$, respectively (Fig. 11(b)). The high activity was attributed to small $M_3C$ nanocrystals (<20 nm) and the microporous structure of $M_3C$-GNRs promoting charge/mass transfer.

Single-crystal metallic interweaved $V_8C_7$ showed Pt-like catalytic efficiency [95]. First, $NH_4VO_3$ nanosheets on nickel foam were coated with glucose polymer to prevent overgrowth, then converted to vanadium oxide (VO). VO@GC was then reduced to single-crystalline $V_8C_7$@GC NSs (Fig. 11(c)). The crystal mismatch

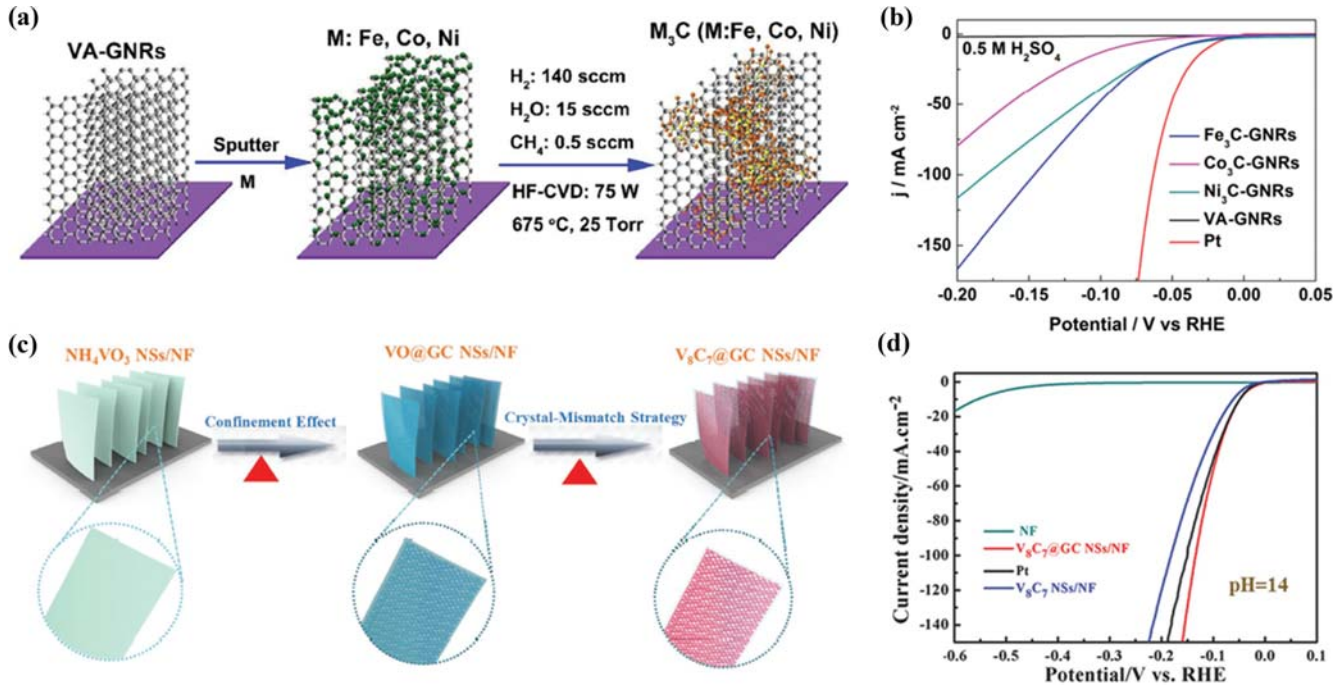


**Fig. 11. (a) Schematic of the synthesis of nanocrystalline $M_3C$ on VA-GNRs and (b) HER polarization curves (in 0.5 M $H_2SO_4$) of $M_3C$-GNRs (Reproduced with permission from Ref. [36], Copyright 2015, American Chemical Society). (c) Schematic of $V_8C_7$@GC NSs/NF fabrication process and (d) HER polarization curves (in 1.0 M KOH) of $V_8C_7$@GC NSs/NF and control samples (Reproduced with permission from Ref. [95], Copyright 2018, Wiley-VCH).**

between VO and $V_8C_7$ is only 4%, so carburation can transform VO to single-crystalline $V_8C_7$. In 0.5 M $H_2SO_4$, 0.1 M phosphate buffer, and 1.0 M KOH, $V_8C_7$@GC NSs/NF showed superior HER activity with extremely low $\eta_{10}$=(47, 77, and 38 mV) and remarkably small Tafel slopes (44, 64, and 34.5 mV $dec^{-1}$), respectively (Fig. 11(d)). The excellent activity of $V_8C_7$ was ascribed to metallic behavior, single-crystal nature, exposed highly-active (110) facet, beneficial C vacancies, and low barrier energy for water dissociation.

## CONCLUSIONS AND OUTLOOK

TMCs have been evaluated as alternatives to Pt-group metals (PGMs) for HER catalyst. Much research has considered molybdenum carbides and tungsten carbides due to their good HER activity. Initial reports showed promise but the activity was fundamentally limited. Various catalyst-design strategies reduced the difference in the activities between PGM and TMC. This review provides examples of four of these approaches.

One of the biggest problems in designing TMC catalysts is their low density of active sites. High carburization temperature induces particle agglomeration and structural collapse to yield bulk materials. To overcome this problem, diverse nano-engineering techniques were developed. Inorganic-organic complexes (e.g., N-rich precursors, MOF) were used to disperse transition metal nanoparticles. Analogously, the confinement effect of various MOFs could physically isolate nanoparticles even at high temperature. Use of carbon supports is another effective nanostructuring method; well-defined carbon supports provide high surface area and promote dispersed TMC nanoparticles. The high conductivity of carbon supports significantly increases the kinetics of HER. Most of all, the formation of covalent bonding between TMC and carbon support modifies the electrochemical structure of TMC, thus increased HER activity.

Even though Mo and W carbides have Pt-like valence band, the intrinsic activity is insufficient to replace Pt. Thus, the electronic configuration was finely tuned to enhance the thermodynamics of TMCs. Heteroatom doping of d-electron rich transition metal can decrease the density of the unfilled d-band in TMCs, and consequently weaken the excessive H-binding strength. Similarly, heterostructure positively alters the electronic structure at the interface. Heterostructures can also induce synergetic effects between two or more active materials. By controlling the composition of $Mo_xC$ phase with different valences of the metal, the HER activity was increased at moderate metal valence, which has optimal H-binding for HER. However, development of TMC HER catalysts still face challenges.

First, the bridge between theoretical and experimental results is missing [7]. Hydrogen binding strength is accepted to be the main indicator of HER activity. Experimental results provide improved HER activity data and provided proofs of change in electronic structure; thus, optimized $\Delta G_{H^*}$. DFT calculation is generally used to verify the optimized $\Delta G_{H^*}$, but no experimental method to directly measure $\Delta G_{H^*}$ exists. Also, technological limitations impede perfect imitation of a real HER in liquid phase, and exact atomic arrangement of active sites.

Second, the catalyst activity should be tested in a membrane electrode assembly (MEA) or single-cell test. An actual water electrolyzer or fuel cell has significantly different operating conditions than the 3-electrode system, so catalyst does not always perfume well in an MEA as it did in the half-cell test [98]. Most of the papers only provide half-cell test data, but MEA test data should be also provided to prove catalyst feasibility for use as HER catalyst in water electrolyzer [99,100].

Finally, mass production of highly efficient TMC catalyst has seldom been reported [101]. The difference between the activities of TMC and Pt has been greatly reduced. However, catalyst production must be scaled up to realize industrial hydrogen production by water electrolysis. Generally, nanostructuring, which is essential to enhance activity, is difficult to reproduce on a large scale. Although remarkable improvements have increased the feasibility of hydrogen production by water electrolysis, many challenges remain.

## ACKNOWLEDGEMENTS

This research was supported by the Korea Institute of Energy Technology Evaluation and Planning (KETEP) and the Ministry of Trade, Industry & Energy (MOTIE) of the Republic of Korea (No. 20182010600430).

## CONFLICT OF INTEREST

The authors have no conflict of interest.

## REFERENCES

1. M. S. Dresselhaus and I. L. Thomas, *Nature*, **414**, 332 (2001).
2. S. T. Thompson and D. Papageorgopoulos, *Nat. Catal.*, **2**, 558 (2019).
3. X. Zou and Y. Zhang, *Chem. Soc. Rev.*, **44**, 5148 (2015).
4. J. Wang, F. Xu, H. Jin, Y. Chen and Y. Wang, *Adv. Mater.*, **29**, 1605838 (2017).
5. Y. Shi and B. Zhang, *Chem. Soc. Rev.*, **45**, 1529 (2016).
6. D. Merki and X. Hu, *Energy Environ. Sci.*, **4**, 3878 (2011).
7. Q. Gao, W. Zhang, Z. Shi, L. Yang and Y. Tang, *Adv. Mater.*, **31**, 1802880 (2019).
8. P. Xiao, X. Ge, H. Wang, Z. Liu, A. Fisher and X. Wang, *Adv. Funct. Mater.*, **25**, 1520 (2015).
9. D. Voiry, M. Salehi, R. Silva, T. Fujita, M. Chen, T. Asefa, V. B. Shenoy, G. Eda and M. Chhowalla, *Nano Lett.*, **13**, 6222 (2013).
10. J. G. Chen, *Chem. Rev.*, **96**, 1477 (1996).
11. H. H. Hwu and J. G. Chen, *Chem. Rev.*, **105**, 185 (2005).
12. H. Vrubel and X. Hu, *Angew. Chem. Int. Ed.*, **51**, 12703 (2012).
13. J. R. Kitchin, J. K. Nørskov, M. A. Barteau and J. G. Chen, *Catal. Today*, **105**, 66 (2005).
14. Q. Gong, Y. Wang, Q. Hu, J. Zhou, R. Feng, P. N. Duchesne, P. Zhang, F. Chen, N. Han, Y. Li, C. Jin, Y. Li and S.-T. Lee, *Nat. Commun.*, **7**, 13216 (2016).
15. J. Patt, D. J. Moon, C. Phillips and L. Thompson, *Catal. Lett.*, **65**, 193 (2000).
16. E. Furimsky, *Appl. Catal. A Gen.*, **240**, 1 (2003).
17. B. Dhandapani, T. St. Clair and S. T. Oyama, *Appl. Catal. A Gen.*, **168**, 219 (1998).
18. S. Wirth, F. Harnisch, M. Weinmann and U. Schröder, *Appl. Catal.*

*B Environ.*, **126**, 225 (2012).
19. J. Wei, M. Zhou, A. Long, Y. Xue, H. Liao, C. Wei and Z. J. Xu, *Nano-Micro Lett.*, **10**, 75 (2018).
20. I. Ledezma-Yanez, W. D. Z. Wallace, P. Sebastián-Pascual, V. Climent, J. M. Feliu and M. T. M. Koper, *Nat. Energy*, **2**, 17031 (2017).
21. J. Luo, J.-H. Im, M. T. Mayer, M. Schreier, M. K. Nazeeruddin, N.-G. Park, S. D. Tilley, H. J. Fan and M. Gratzel, *Science*, **345**, 1593 (2014).
22. B. E. Conway and B. V. Tilak, *Electrochim. Acta*, **47**, 3571 (2002).
23. R. Michalsky, Y.-J. Zhang and A. A. Peterson, *ACS Catal.*, **4**, 1274 (2014).
24. S. T. Oyama, J. C. Schlatter, J. E. Metcalfe and J. M. Lambert, *Ind. Eng. Chem. Res.*, **27**, 1639 (1988).
25. J. Lu, H. Hugosson, O. Eriksson, L. Nordström and U. Jansson, *Thin Solid Films*, **370**, 203 (2000).
26. T. Hyeon, M. Fang and K. S. Suslick, *J. Am. Chem. Soc.*, **118**, 5492 (1996).
27. W.-F. Chen, C.-H. Wang, K. Sasaki, N. Marinkovic, W. Xu, J. T. Muckerman, Y. Zhu and R. R. Adzic, *Energy Environ. Sci.*, **6**, 943 (2013).
28. Y. Zhao, K. Kamiya, K. Hashimoto and S. Nakanishi, *J. Am. Chem. Soc.*, **137**, 110 (2015).
29. S. T. Hunt, T. Nimmanwudipong and Y. Román-Leshkov, *Angew. Chem. Int. Ed.*, **53**, 5131 (2014).
30. S. T. Hunt, M. Milina, A. C. Alba-Rubio, C. H. Hendon, J. A. Dumesic and Y. Roman-Leshkov, *Science*, **352**, 974 (2016).
31. L. J. Kecskes and A. Niiler, *J. Am. Ceram. Soc.*, **72**, 655 (1989).
32. J. S. Lee, S. T. Oyama and M. Boudart, *J. Catal.*, **106**, 125 (1987).
33. C. Wan, Y. N. Regmi and B. M. Leonard, *Angew. Chem. Int. Ed.*, **53**, 6407 (2014).
34. J. B. Claridge, A. P. E. York, A. J. Brungs and M. L. H. Green, *Chem. Mater.*, **12**, 132 (2000).
35. Z. Wu, Y. Yang, D. Gu, Q. Li, D. Feng, Z. Chen, B. Tu, P. A. Webley and D. Zhao, *Small*, **5**, 2738 (2009).
36. X. Fan, Z. Peng, R. Ye, H. Zhou and X. Guo, *ACS Nano*, **9**, 7407 (2015).
37. J. Hojo, R. Oono and A. Kato, *J. Mater. Sci.*, **15**, 2335 (1980).
38. H. T. Kim, S.-Y. Lee, H.-R. Lee and C. Park, *Korean J. Chem. Eng.*, **35**, 246 (2018).
39. Q. Gao, N. Liu, S. Wang and Y. Tang, *Nanoscale*, **6**, 14106 (2014).
40. R. Ma, Y. Zhou, Y. Chen, P. Li, Q. Liu and J. Wang, *Angew. Chem. Int. Ed.*, **54**, 14723 (2015).
41. H. Lin, Z. Shi, S. He, X. Yu, S. Wang, Q. Gao and Y. Tang, *Chem. Sci.*, **7**, 3399 (2016).
42. S. Kim, C. Choi, J. Hwang, J. Park, J. Jeong, H. Jun, S. Lee, S.-K. Kim, J. H. Jang, Y. Jung and J. Lee, *ACS Nano*, **14**, 4988 (2020).
43. X. Fan, H. Zhou and X. Guo, *ACS Nano*, **9**, 5125 (2015).
44. J.-S. Li, Y. Wang, C.-H. Liu, S.-L. Li, Y.-G. Wang, L.-Z. Dong, Z.-H. Dai, Y.-F. Li and Y.-Q. Lan, *Nat. Commun.*, **7**, 1 (2016).
45. N. Han, K. R. Yang, Z. Lu, Y. Li, W. Xu, T. Gao, Z. Cai, Y. Zhang, V. S. Batista, W. Liu and X. Sun, *Nat. Commun.*, **9**, 1 (2018).
46. H. Lin, N. Liu, Z. Shi, Y. Guo, Y. Tang and Q. Gao, *Adv. Funct. Mater.*, **26**, 5590 (2016).
47. F. Yu, Y. Gao, Z. Lang, Y. Ma, L. Yin, J. Du, H. Tan, Y. Wang and Y. Li, *Nanoscale*, **10**, 6080 (2018).
48. C. Wan and B. M. Leonard, *Chem. Mater.*, **27**, 4281 (2015).
49. Y.-Y. Chen, Y. Zhang, W.-J. Jiang, X. Zhang, Z. Dai, L.-J. Wan and J.-S. Hu, *ACS Nano*, **10**, 8851 (2016).
50. S. Bukola, B. Merzougui, A. Akinpelu and M. Zeama, *Electrochim. Acta*, **190**, 1113 (2016).
51. T. Y. Ma, J. L. Cao, M. Jaroniec and S. Z. Qiao, *Angew. Chem. Int. Ed.*, **55**, 1138 (2016).
52. K. Zhang, Y. Zhao, S. Zhang, H. Yu, Y. Chen, P. Gao and C. Zhu, *J. Mater. Chem. A*, **2**, 18715 (2014).
53. H. Yan, Y. Xie, Y. Jiao, A. Wu, C. Tian, X. Zhang, L. Wang and H. Fu, *Adv. Mater.*, **30**, 1704156 (2018).
54. A. Nilsson, L. G. M. Pettersson, B. Hammer, T. Bligaard, C. H. Christensen and J. K. Nørskov, *Catal. Lett.*, **100**, 111 (2005).
55. Y. Gao, Z. Lang, F. Yu, H. Tan, G. Yan, Y. Wang, Y. Ma and Y. Li, *ChemSusChem*, **11**, 1082 (2018).
56. L. He, W. Zhang, Q. Mo, W. Huang, L. Yang and Q. Gao, *Angew. Chem. Int. Ed.*, **59**, 3544 (2020).
57. X. Zhang, J. Wang, T. Guo, T. Liu, Z. Wu, L. Cavallo, Z. Cao and D. Wang, *Appl. Catal. B Environ.*, **247**, 78 (2019).
58. Q. Gong, Y. Wang, Q. Hu, J. Zhou, R. Feng, P. N. Duchesne, P. Zhang, F. Chen, N. Han, Y. Li, C. Jin, Y. Li and S.-T. Lee, *Nat. Commun.*, **7**, 13216 (2016).
59. J. R. dos S. Politi, F. Viñes, J. A. Rodriguez and F. Illas, *Phys. Chem. Chem. Phys.*, **15**, 12617 (2013).
60. C. Giordano, C. Erpen, W. Yao and M. Antonietti, *Nano Lett.*, **8**, 4659 (2008).
61. W.-F. Chen, S. Iyer, S. Iyer, K. Sasaki, C.-H. Wang, Y. Zhu, J. T. Muckerman and E. Fujita, *Energy Environ. Sci.*, **6**, 1818 (2013).
62. Y. Huang, J. Ge, J. Hu, J. Zhang, J. Hao and Y. Wei, *Adv. Energy Mater.*, **8**, 1701601 (2018).
63. Y. Liu, G. Yu, G.-D. Li, Y. Sun, T. Asefa, W. Chen and X. Zou, *Angew. Chem. Int. Ed.*, **54**, 10752 (2015).
64. Y.-R. Lee, J. Kim and W.-S. Ahn, *Korean J. Chem. Eng.*, **30**, 1667 (2013).
65. N. M. Mahmoodi, M. Taghizadeh and A. Taghizadeh, *Korean J. Chem. Eng.*, **36**, 287 (2019).
66. R. Kim, S. Jee, U. Ryu, H. S. Lee, S. Y. Kim and K. M. Choi, *Korean J. Chem. Eng.*, **36**, 975 (2019).
67. P. Kumar, E. Vejerano, A. Khan, G. Lisak, J. H. Ahn and K.-H. Kim, *Korean J. Chem. Eng.*, **36**, 1839 (2019).
68. H. B. Wu, B. Y. Xia, L. Yu, X.-Y. Yu and X. W. Lou, *Nat. Commun.*, **6**, 6512 (2015).
69. H. Zhang, Z. Ma, G. Liu, L. Shi, J. Tang, H. Pang, K. Wu, T. Takei, J. Zhang, Y. Yamauchi and J. Ye, *NPG Asia Mater.*, **8**, e293 (2016).
70. P. Liu and J. K. Nørskov, *Phys. Chem. Chem. Phys.*, **3**, 3814 (2001).
71. D. H. Youn, S. Han, J. Y. Kim, J. Y. Kim, H. Park, S. H. Choi and J. S. Lee, *ACS Nano*, **8**, 5164 (2014).
72. A. M. Gómez–Marín and E. A. Ticianelli, *Appl. Catal. B Environ.*, **209**, 600 (2017).
73. Z. Shi, K. Nie, Z.-J. Shao, B. Gao, H. Lin, H. Zhang, B. Liu, Y. Wang, Y. Zhang, X. Sun, X.-M. Cao, P. Hu, Q. Gao and Y. Tang, *Energy Environ. Sci.*, **10**, 1262 (2017).
74. C. Tang, W. Wang, A. Sun, C. Qi, D. Zhang, Z. Wu and D. Wang, *ACS Catal.*, **5**, 6956 (2015).
75. Y. Zheng, Y. Jiao, M. Jaroniec and S. Z. Qiao, *Angew. Chem. Int. Ed.*, **54**, 52 (2015).
76. Y. Zheng, Y. Jiao, L. H. Li, T. Xing, Y. Chen, M. Jaroniec and S. Z. Qiao, *ACS Nano*, **8**, 5290 (2014).

77. G. Zhao, K. Rui, S. X. Dou and W. Sun, *Adv. Funct. Mater.*, **28**, 1803291 (2018).
78. Y. N. Regmi, A. Roy, G. A. Goenaga, J. R. McBride, B. R. Rogers, T. A. Zawodzinski, N. Labbé and S. C. Chmely, *ChemCatChem*, **9**, 1054 (2017).
79. T. Liu, X. Zhang, T. Guo, Z. Wu and D. Wang, *Electrochim. Acta*, **334**, 135624 (2020).
80. Y. Liu, B. Huang and Z. Xie, *Appl. Surf. Sci.*, **427**, 693 (2018).
81. H. Zhang, H. Jin, Y. Yang, F. Sun, Y. Liu, X. Du, S. Zhang, F. Song, J. Wang, Y. Wang and Z. Jiang, *J. Energy Chem.*, **35**, 66 (2019).
82. R. B. Levy and M. Boudart, *Science*, **181**, 547 (1973).
83. Y.-T. Xu, X. Xiao, Z.-M. Ye, S. Zhao, R. Shen, C.-T. He, J.-P. Zhang, Y. Li and X.-M. Chen, *J. Am. Chem. Soc.*, **139**, 5285 (2017).
84. G. Yan, C. Wu, H. Tan, X. Feng, L. Yan, H. Zang and Y. Li, *J. Mater. Chem. A*, **5**, 765 (2017).
85. Y.-J. Ko, J.-M. Cho, I. Kim, D. S. Jeong, K.-S. Lee, J.-K. Park, Y.-J. Baik, H.-J. Choi and W.-S. Lee, *Appl. Catal. B Environ.*, **203**, 684 (2017).
86. B. Ren, D. Li, Q. Jin, H. Cui and C. Wang, *J. Mater. Chem. A*, **5**, 13196 (2017).
87. J. Shi, Z. Pu, Q. Liu, A. M. Asiri, J. Hu and X. Sun, *Electrochim. Acta*, **154**, 345 (2015).
88. S. M. Schmuecker, D. Clouser, T. J. Kraus and B. M. Leonard, *Dalton T.*, **46**, 13524 (2017).
89. A. Ignaszak, C. Song, W. Zhu, J. Zhang, A. Bauer, R. Baker, V. Neburchilov, S. Ye and S. Campbell, *Electrochim. Acta*, **69**, 397 (2012).
90. A. A. Edigaryan, V. A. Safonov, E. N. Lubnin, L. N. Vykhodtseva, G. E. Chusova and Y. M. Polukarov, *Electrochim. Acta*, **47**, 2775 (2002).
91. P. R. Deshmukh, H. S. Hyun, Y. Sohn and W. G. Shin, *Korean J. Chem. Eng.*, **37**, 546 (2020).
92. W.-F. Chen, J. T. Muckerman and E. Fujita, *Chem. Commun.*, **49**, 8896 (2013).
93. S. Li, C. Yang, Z. Yin, H. Yang, Y. Chen, L. Lin, M. Li, W. Li, G. Hu and D. Ma, *Nano Res.*, **10**, 1322 (2017).
94. L. Zhang, Y. Chen, P. Zhao, W. Luo, S. Chen and M. Shao, *Electrocatalysis*, **9**, 264 (2018).
95. H. Xu, J. Wan, H. Zhang, L. Fang, L. Liu, Z. Huang, J. Li, X. Gu and Y. Wang, *Adv. Energy Mater.*, **8**, 1800575 (2018).
96. S. Lee, M. Choun, Y. Ye, J. Lee, Y. Mun, E. Kang, J. Hwang, Y.-H. Lee, C.-H. Shin, S.-H. Moon, S.-K. Kim, E. Lee and J. Lee, *Angew. Chem. Int. Ed.*, **54**, 9230 (2015).
97. Y. Mun, M. J. Kim, S.-A. Park, E. Lee, Y. Ye, S. Lee, Y.-T. Kim, S. Kim, O.-H. Kim, Y.-H. Cho, Y.-E. Sung and J. Lee, *Appl. Catal. B Environ.*, **222**, 191 (2018).
98. D. Joo, K. Han, J. H. Jang and S. Park, *Korean J. Chem. Eng.*, **36**, 299 (2019).
99. M. A. R. Anjum, M. H. Lee and J. S. Lee, *ACS Catal.*, **8**, 8296 (2018).
100. J. Xing, Y. Li, S. Guo, T. Jin, H. Li, Y. Wang and L. Jiao, *Electrochim. Acta*, **298**, 305 (2019).
101. D. Y. Chung, S. W. Jun, G. Yoon, H. Kim, J. M. Yoo, K.-S. Lee, T. Kim, H. Shin, A. K. Sinha, S. G. Kwon, K. Kang, T. Hyeon and Y.-E. Sung, *J. Am. Chem. Soc.*, **139**, 6669 (2017).

Jinwoo Lee received his B.S., M.S. and Ph.D degrees from the Department of Chemical and Biological Engineering of Seoul National University (SNU), Korea, in 1998, 2000, and 2003, respectively. After postdoctoral research at SNU (with Prof. Taeghwan Hyeon) and Cornell University (with Prof. Ulrich Wiesner), he joined the faculty of the Department of Chemical Engineering at Pohang University of Science and Technology (POSTECH) (2008-2018). In 2018, he joined the faculty of the Department of Chemical and Biomolecular Engineering at Korea Advanced Institute of Science and Technology (KAIST). He is interested in the synthesis and application of designed nano-functional materials for energy conversion and storage devices.